

A NEW SAMPLE OF BURIED ACTIVE GALACTIC NUCLEI SELECTED FROM THE SECOND *XMM-NEWTON* SERENDIPITOUS SOURCE CATALOGUE

KAZUHISA NOGUCHI, YUICHI TERASHIMA, AND HISAMITSU AWAKI

Department of Physics, Ehime University, Matsuyama, Ehime 790-8577, Japan

To appear in The Astrophysical Journal.

ABSTRACT

We present the results of X-ray spectral analysis of 22 active galactic nuclei (AGNs) with a small scattering fraction selected from the Second *XMM-Newton* Serendipitous Source Catalogue using hardness ratios. They are candidates of buried AGNs, since a scattering fraction, which is a fraction of scattered emission by the circumnuclear photoionized gas with respect to direct emission, can be used to estimate the size of the opening part of an obscuring torus. Their X-ray spectra are modeled by a combination of a power law with a photon index of 1.5–2 absorbed by a column density of $\sim 10^{23\text{--}24} \text{ cm}^{-2}$, an unabsorbed power law, narrow Gaussian lines, and some additional soft components. We find that scattering fractions of 20 among 22 objects are less than a typical value ($\sim 3\%$) for Seyfert2s observed so far. In particular, those of eight objects are smaller than 0.5%, which are in the range for buried AGNs found in recent hard X-ray surveys. Moreover, [O III] $\lambda 5007$ luminosities at given X-ray luminosities for some objects are smaller than those for Seyfert2s previously known. This fact could be interpreted as a smaller size of optical narrow emission line regions produced in the opening direction of the obscuring torus. These results indicate that they are strong candidates for the AGN buried in a very geometrically thick torus.

Subject headings: galaxies: active, galaxies: Seyfert, X-rays: galaxies

1. INTRODUCTION

It is widely accepted that the cosmic X-ray background (CXB) is produced by the integrated emission of faint extragalactic pointlike sources (Brandt & Hasinger 2005). *XMM-Newton* and *Chandra* resolved 80%–100% of the CXB at $< 2 \text{ keV}$, while the resolved fraction of the CXB at hard X-rays (8–12 keV) decreased to only $\approx 50\%$ (Worsley et al. 2005). Various observations indicate that a large fraction of active galactic nuclei (AGNs) is hidden by a large amount of cold material (e.g., Awaki et al. 1991; Comastri 2004). According to population synthesis models of the CXB (Comastri et al. 1995; Ueda et al. 2003; Gilli et al. 2007), the peak intensity of the CXB spectrum at 30 keV can be explained by considering contribution of hidden AGNs. Such a population is yet to be understood, because the direct emission from the nucleus is absorbed by surrounding cold gas and is hard to be fully explored with X-ray observations below 10 keV. Hard X-ray surveys performed with *Swift/BAT* (15–200 keV; Markwardt et al. 2005; Tueller et al. 2008) and *INTEGRAL* (10–100 keV; Bassani et al. 2006; Beckmann et al. 2006; Sazonov et al. 2007) are suitable for unveiling such a type of AGNs with much less selection biases than surveys at lower energies. In fact, AGNs buried in a large amount of matter have been discovered by *Suzaku* follow up observations of a sample selected by the *Swift/BAT* survey (Ueda et al. 2007).

In a unified model of an AGN (e.g., Antonucci 1993), torus-like gas is surrounding a supermassive black hole (SMBH), and photoionized gas is created in the opening part of the torus by radiation from the nucleus. If an AGN is observed from the torus side, absorbed direct emission and scattered light by the photoionized gas will be observed in an X-ray spectrum. The fraction of scattered light to direct emission (scattering fraction) can be used to estimate the opening angle of the torus. The fractions for AGNs found by Ueda et al (2007) are extremely small ($< 0.5\%$), whereas a typical value is $\sim 3\%$ (Turner et al. 1997; Bianchi and Guainazzi 2007). Fur-

thermore, Winter et al (2008) found a similar type of AGNs by *XMM-Newton* observations of *Swift/BAT* selected AGNs. They would be buried in a geometrically thick torus with a very small opening angle assuming that the scattering fraction reflects the solid angle of the opening part of the torus. In an early stage of the evolution of galaxies and their central black holes, a large amount of gas responsible for active star formation may be closely related to obscuration of the nucleus. Therefore, AGNs almost fully covered by an absorber are an important class of objects in studying evolution of AGNs and their hosts. Moreover, they might be significant contributors to the CXB at hard X-rays. Testing a selection technique to find such AGNs and understanding the properties of the population are of significant interest for exploring these issues.

We search for buried AGNs with a scattering fraction of 0.5% or less using the Second *XMM-Newton* Serendipitous Source Catalogue (2XMM) and the archival data of *XMM-Newton*. We selected candidate sources from the catalogue using hardness ratios (HRs) and scattering fractions calculated by analyzing spectra obtained with *XMM-Newton*. The selection method of candidate sources is described in Section 2. Our results of spectral analysis are presented in Section 3 and their characteristics are discussed in Section 4. Section 5 summarizes our conclusions. We adopt $(H_0, \Omega_m, \Omega_\lambda) = (70 \text{ km s}^{-1} \text{Mpc}^{-1}, 0.3, 0.7)$ throughout this paper.

2. SELECTION OF CANDIDATES FOR A BURIED AGN

Our sample was selected from the 2XMM Catalogue that has been assembled by the *XMM-Newton* Survey Science Centre (Watson et al. 2009). This catalogue contains 246897 X-ray source detections. The median flux in the full energy band (0.2–12 keV) is $\sim 2.5 \times 10^{-14} \text{ erg cm}^{-2} \text{ s}^{-1}$ and about 20% of the sources have total fluxes below $1 \times 10^{-14} \text{ erg cm}^{-2} \text{ s}^{-1}$.

We used HR3 and HR4 among some HRs defined in the 2XMM Catalogue to select candidates of buried AGNs. These

HRs are defined as

$$HR3 = \frac{CR(2.0-4.5 \text{ keV}) - CR(1.0-2.0 \text{ keV})}{CR(2.0-4.5 \text{ keV}) + CR(1.0-2.0 \text{ keV})}$$

and

$$HR4 = \frac{CR(4.5-12 \text{ keV}) - CR(2.0-4.5 \text{ keV})}{CR(4.5-12 \text{ keV}) + CR(2.0-4.5 \text{ keV})},$$

where $CR(1.0-2.0 \text{ keV})$, $CR(2.0-4.5 \text{ keV})$, and $CR(4.5-12 \text{ keV})$ are count rates in the 1.0–2.0, 2.0–4.5, and 4.5–12 keV bands, respectively. The values of HR given in the 2XMM Catalogue were calculated using count rates measured by the `emldetect` task in the *XMM-Newton* Science Analysis System (SAS). If direct emission from an AGN is absorbed by cold material with $N_H \sim 10^{23} \text{ cm}^{-2}$, $CR(1.0-2.0 \text{ keV})$ and $CR(2.0-4.5 \text{ keV})$ are dominated by the soft component such as scattered emission and absorbed direct emission, respectively. In the case of $N_H \sim 10^{24} \text{ cm}^{-2}$, $CR(2.0-4.5 \text{ keV})$ and $CR(4.5-12 \text{ keV})$ are dominated by the soft component and direct emission, respectively. Therefore, HR3 and HR4 can be used to efficiently select objects with $N_H \sim 10^{23} \text{ cm}^{-2}$ and 10^{24} cm^{-2} , respectively.

In the selection process, we required sources to satisfy the following conditions: 1) count rate for EPIC-pn in 0.2–12 keV $> 0.05 \text{ cts s}^{-1}$, 2) high Galactic latitude ($|b| > 20^\circ$), and 3) error of HRs ≤ 0.2 at a 90% confidence level. The errors of HRs shown in the 2XMM Catalogue were derived from count rates measured by the SAS task `emldetect`. 4627 sources among 246897 satisfied these criteria.

We simulated AGN spectra in XSPEC (version 11.2) to calculate HRs expected for an object with a low scattering fraction, using the response function of the EPIC-pn. The spectral model assumed in the simulation is a combination of absorbed and unabsorbed power laws, which correspond to direct and scattered components, respectively. We fixed the photon indices of both power-law components at 1.9, which is a typical value of Seyfert 2 galaxies (e.g., Smith & Done 1996). The scattering fraction is defined as a ratio between the normalizations of the two power laws. We simulated spectra for scattering fractions of 10, 5, 3, 1, and 0.5%, and $\log N_H$ from 20.5 to 24.5 cm^{-2} at a logarithmic step of 0.1. The expected HRs are shown in Figure 1 as solid and dashed lines. The five solid lines represent the scattering fractions of 10, 5, 3, 1, and 0.5% from inside to outside. The three dashed lines correspond to objects with $\log N_H = 23, 23.5$, and 24 from lower right to upper left. 4627 sources, which fulfilled the conditions defined above, are also plotted as crosses. Objects with a small scattering fraction are located in the upper right portion in this figure.

In order to select buried AGNs with a scattering fraction of $< 0.5\%$ as many as possible, we selected 23 objects located upper right of the line for a scattering fraction of 1% since there are uncertainties in HR values and all the spectra may not be explained by the simple model defined above. The 23 candidates are plotted with circles in Figure 1. In Table 1, we list the source name, AGN type, redshift, Galactic column density toward the source, start date of the observation, exposure time after data screening given in Section 3, and count rates in the 0.4–10 keV band. References for the AGN type are also shown in Table 1. Redshifts are taken from NASA/IPAC Extragalactic Database (NED). The criteria adopted in this paper to select a buried AGN hold at low redshift only, because we assumed $z = 0$ in the simulation of

AGN spectra used to calculate the expected HRs. In fact, most of AGNs in our sample are at $z < 0.1$. The Galactic column densities are calculated from 21 cm measurements (Kalberla et al. 2005) using the `nh` tool at the NASA’s High Energy Astrophysics Science Archive Research Center. *XMM-Newton* results of some of the objects in our sample have been published. References for them are listed in Table 1. Since 2XMM J234349.7–151700 is a star, we excluded it from our sample for spectral analysis in Section 3.

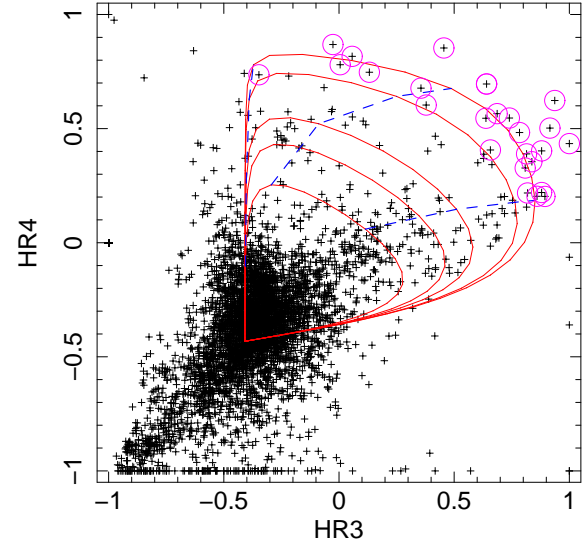


FIG. 1.— Distribution of HR for the 2XMM Catalogue sources (Crosses). These are satisfied all conditions; count rate in 0.2–12 keV $> 0.05 \text{ cts s}^{-1}$, $|b| > 20^\circ$, and HR error ≤ 0.2 . Our sample is shown by circles. Solid lines show the HRs expected for the scattering fraction of 10, 5, 3, 1, and 0.5% from inside to outside. Dashed lines correspond to $\log N_H = 23, 23.5$, and 24 cm^{-2} from lower right to upper left.

3. DATA REDUCTION AND ANALYSIS

In order to calculate accurate values of the scattering fraction for our sample, we analyzed their X-ray spectra obtained with EPIC-pn. The data were reduced with the SAS version 7.1. We created calibrated photon event files for the EPIC-pn camera from the observation data files (ODF). The ancillary response files and detector response matrices were generated using the `arfgen` and `rmfgen` tasks, respectively. X-ray events corresponding to patterns 0–4 were selected from the event files. We extracted source spectra from circular regions with a radius in a range $10''$ – $40''$, depending on the brightness of the source. Background spectra were taken from a region near the target. Time intervals with very high background rates were identified in light curves above 10 keV and discarded. We fit spectra of the sample in the 0.4–10 keV range with various models by using XSPEC version 11.2. All spectra except one were binned so that each spectral bin contains more than 20 counts per bin to enable usage of the χ^2 fit statistics. Since the total number of counts for one object, 2MASX J12544196–3019224, is small, the same way of binning resulted in very small number of bins. We therefore used C -statistic (Cash 1979) to fit the unbinned spectrum of this object. The quoted errors correspond to a 90% confidence level for one interesting parameter (i.e., $\Delta\chi^2$ or $\Delta C = 2.71$).

TABLE 1
PROPERTIES OF SAMPLE

2XMM Name	Other Name	Class ^a	Reference ^b	Redshift ^c	N_{H}^d (10^{20} cm^{-2})	Start Date	Exposure ^e (s)	Count Rate ^f (counts s^{-1})	Reference ^g
2XMM J004847.1+315724	Mrk 348	Sy2	1	0.015034	5.79	2002 Jul 18	19323	2.0	6,7
2XMM J010852.8+132015	3C 33	Sy2	2	0.059700	3.23	2004 Jan 21	6291	0.19	8,9
2XMM J022813.4–031502	2MASX J02281350–0315023	0.078706 ^h	2.21	2002 Jul 26	8487	0.040	...
2XMM J025512.1–001100	NGC 1142	Sy2	1	0.028847	5.81	2006 Jan 28	8879	0.23	10
2XMM J035854.4+102602	3C 98	Sy2	1	0.030454	10.2	2002 Sep 07	13771	0.22	11
2XMM J090053.8+385616	B2 0857+39	Sy2	3	0.229000	2.05	2004 Apr 13	20151	0.013	...
2XMM J091957.9+371127	IC 2461	0.007539	1.08	2003 Apr 15	48567	0.19	...
2XMM J103352.6+004403	2MASX J10335255+0044033	Sy1.8	1	0.131500	4.81	2005 Dec 11	4391	0.048	...
2XMM J113543.9+490216	MCG+08–21–065	0.029687	1.75	2003 Nov 24	15007	0.029	...
2XMM J120429.7+201858	NGC 4074	Sy2	1	0.022445	2.30	2003 Jan 02	2767	0.11	...
2XMM J120929.7+434106	NGC 4138	Sy1.9	4	0.002962	1.25	2001 Nov 26	8801	0.45	12,13
2XMM J122546.7+123943	NGC 4388	Sy1.9	4	0.008419	2.58	2002 Dec 12	7346	1.5	14
2XMM J123536.6–395433	NGC 4507	Sy2	1	0.011801	7.04	2001 Jan 04	34020	0.99	15
2XMM J123854.6–271827	ESO 506–G027	Sy2	5	0.025024	5.45	2006 Jan 24	8276	0.22	10
2XMM J125442.6–301928	2MASX J12544196–3019224	0.056105	5.99	2004 Jan 15	10314	0.013	...
2XMM J130414.3–102021	NGC 4939	Sy2	1	0.010374	3.30	2002 Jan 03	11503	0.050	16
2XMM J133326.1–340052	ESO 383–G18	Sy1.8	1	0.012412	4.04	2006 Jan 10	12573	0.43	...
2XMM J183820.3–652539	ESO 103–G035	Sy2	1	0.013286	5.71	2002 Mar 15	8392	1.6	17,18
2XMM J201958.9–523718	IC 4995	Sy2	1	0.016094	4.08	2004 Sep 25	6630	0.068	19
2XMM J213147.2–425051	NGC 7070A	0.007976	2.56	2004 Oct 28	26377	0.15	20
2XMM J220201.8–315210	NGC 7172	Sy2	1	0.008683	1.95	2007 Apr 24	27833	3.4	6
2XMM J223603.5+335833	NGC 7319	Sy2	1	0.022507	6.15	2001 Dec 07	34010	0.11	21
2XMM J234349.7–151700	R Aqr	1.87	2005 Jul 30

REFERENCES. — (1)Veron-Cetty & Veron 2006; (2)Fanaroff & Riley 1974; (3)Kiuchi et al 2006; (4)Ho et al. 1997; (5)Tueller et al 2008; (6)Awaki et al. 2006; (7)Guainazzi & Bianchi 2007; (8)Evans et al. 2006; (9)Kraft et al 2007; (10)Winter et al. 2008; (11)Isobe et al. 2005; (12)Foschini et al. 2002; (13)Cappi et al. 2006; (14)Beckmann et al. 2004; (15)Matt et al. 2004; (16)Guainazzi et al 2005a; (17)Shinozaki et al 2006; (18)De Rosa et al 2008; (19)Guainazzi et al. 2005b; (20)Trinchieri et al. 2008; (21)Trinchieri et al. 2005.

^a Optical classification. “Sy2” represents Seyfert 2. “Sy1.8” and “Sy1.9” represent intermediate Seyfert.

^b References for optical classification.

^c Redshift are taken from the NED, expect for 2MASX J02281350–0315023.

^d Galactic column density by 21 cm measurement (Kalberla et al. 2005).

^e Cleaned exposure of EPIC-pn.

^f Count rate in the 0.4–10 keV band.

^g References for published *XMM-Newton* results.

^h Determined by an Fe–K α emission line in the X-ray spectrum analyzed in this paper. The line center energy is assumed to be 6.4 keV in the source rest frame.

3.1. Baseline Model

We fitted spectra of the 22 sources with a model consisting of two power laws and a narrow Gaussian line to account for an Fe K emission at 6.4 keV, all modified by Galactic absorption using phabs in XSPEC. An absorption by cold matter at the redshift of the source (zphabs in XSPEC) was added to the Gaussian and one of the power laws. We assumed that the photon indices of both power laws are same. Hereafter, we refer to this model as the baseline model. Of 22 sources, spectra of seven sources (2MASX J02281350–0315023, B2 0857+39, 2MASX J10335255+0044033, MCG +08–21–065, NGC 4074, 2MASX J12544196–3019224, and NGC 7070A) are well fitted with the baseline model. In these fits, the photon indices (Γ) were fixed at 1.9 except for NGC 7070A, since uncertainties of Γ became large ($> 20\%$) if Γ was left free. The results are shown in Table 2. The best-fit N_{H} values for the seven objects are about $2 \times 10^{23} \text{ cm}^{-2}$. The spectra of these objects are shown in Figure 2.

3.2. Complex Models

Spectra of 15 sources were not satisfactorily fitted with the baseline model. They showed soft X-ray excess below ~ 2 keV and/or residuals between 2 and 4 keV. We added extra components modified by Galactic absorption to the baseline model until good fits were obtained. The photon indices for NGC 4939 and IC 4995 were fixed at 1.9, since uncertainties of Γ were large if Γ was left free.

First, we added an optically thin thermal plasma model (mekal model in XSPEC; Mewe et al. 1985; Kaastra 1992; Liedahl et al. 1995) to the baseline model. The abundance was fixed at 0.5 solar, where the solar abundance table by Anders and Grevesse (1989) was assumed. If the temperature of the plasma was not constrained, the value was fixed at 0.65 keV, which is typically observed in Seyfert 2 (e.g., Guainazzi et al. 2005b). Spectra of six objects (NGC 1142, 3C 98, IC 2461, NGC 4138, NGC 4939, and NGC 7172) were fitted acceptably with this model. In the spectrum of NGC 7172, excess emission at around 1.7 keV was seen in this model fit ($\chi^2_{\nu}(\text{dof}) = 1.27(170)$). We added a second Gaussian component in order to account for this feature, and obtained an improved fit ($\chi^2_{\nu}(\text{dof}) = 1.18(168)$). Soft excess seen in the spectrum of IC 4995 was modeled by adding a second mekal component ($\chi^2_{\nu}(\text{dof}) = 1.14(15)$). The best-fit temperatures of the two mekal components are $kT \approx 0.08$ and ≈ 0.5 keV, respectively.

Next, we added a Compton reflection model (pexrav in XSPEC; Magdziarz & Zdziarski 1995) to the baseline model. We fixed the inclination angle of the reflector at 60° (0° corresponds to face-on), the high-energy cutoff of the incident power law at 300 keV, and assumed solar abundances (Anders & Grevesse 1989). The pexrav model was used in such a way that it produces reflected emission only (rel_{refl} parameter was set to -1 in XSPEC) since the direct component was modeled by an absorbed power law. The normalization and Γ of pexrav were assumed to be the same as those of the absorbed power-law component. This model was applied to the remaining eight objects. If the absorption column for the reflection component was left free, the spectrum of ESO 506–G027 was reproduced by this model. The spectrum of other objects was not explained by adding this model component.

In order to represent the spectra of the remaining seven sources, both mekal and pexrav were added to the baseline

model. The spectra of 3C 33, and ESO 383–G18 were explained by this model. If the absorption column for the reflection component was left free, the spectra of ESO 103–G035 and NGC 7319 were reproduced. If two mekal components ($kT \approx 0.2$ and ≈ 0.8 keV) and absorbed pexrav were introduced, the spectrum of NGC 4388 was explained.

Mrk 348 and NGC 4507 show more complex X-ray spectral shapes that were not reproduced by the models explained above. In the fit of the spectrum of Mrk 348, we added two mekal components and the third absorbed power law to the baseline model. The photon indices of all the power-law components were assumed to be the same. Moreover, two Gaussians with negative normalization were also added to represent two absorption-line like features seen at 6.6 keV and 6.9 keV. This model provided an acceptable fit to the spectrum of Mrk 348. In order to represent the spectrum of NGC 4507, we introduced the following model components. We used nine Gaussians instead of mekal to model the soft part of the spectrum. A Gaussian to express the Compton shoulder (CS; see Matt 2002) was also added at 6.32 keV with a fixed width of $\sigma = 40$ eV as in Matt et al. (2004). An absorbed pexrav component was also added, where the absorption column density for pexrav was assumed to be independent of that for the absorbed power law component. The combination of the baseline model and these additional components reproduced the spectrum.

The results of the fits are summarized in Tables 3, 4, and 5. Table 6 shows the best-fit models for our sample. The photon indices were distributed between ~ 1.5 and 2.0 . This is consistent with a range of photon indices observed in Seyfert 2s (e.g., Smith & Done 1996). The obtained N_{H} were in the range of $\sim 10^{23\text{--}24} \text{ cm}^{-2}$. The spectra along with the best-fit model are shown in Figure 2.

3.3. Fluxes and Luminosities

The X-ray fluxes calculated using the best-fit model are summarized in Table 7. Columns 2 and 3 are observed fluxes in the 0.5–2 keV and 2–10 keV bands, respectively. Columns 4 and 5 are observed fluxes for the power-law components in the 0.5–2 keV and 2–10 keV bands, respectively. Columns 6 and 7 are absorption corrected fluxes for the power-law components in the 0.5–2 keV and 2–10 keV bands, respectively. Columns 8 and 9 are observed and absorption corrected fluxes in the 0.5–2 keV band, respectively, for the power law with only Galactic absorption. Columns 10 and 11 are observed and absorption corrected fluxes, respectively, for the mekal component in the 0.5–2 keV band. We calculated intrinsic luminosities of the absorbed power-law component in the 2–10 keV band as shown in Table 8, Column 2. Most of the objects have luminosities in the range of Seyferts ($10^{41\text{--}44} \text{ erg s}^{-1}$). The intrinsic 0.5–2 keV luminosities for all the components except for the heavily absorbed power law were also calculated and tabulated in Table 8, Column 3.

4. DISCUSSION

4.1. The Origin of the Soft X-ray Emission

Since various spectral components presumably contribute to the soft X-ray emission in obscured AGNs, understanding the origin of the soft emission is of importance to derive true scattering fractions. One of the possible origins is the circumnuclear gas photoionized and photoexcited by AGN emission. The soft X-ray emission is also produced through Thomson scattering of the primary radiation by free electrons

TABLE 2
SPECTRAL PARAMETERS FOR THE BASELINE MODEL

Name	N_{H} (10^{22} cm^{-2})	Γ	A_{int}^a	E_{line} (keV)	σ (eV)	EW (eV)	A_{ga}^b	A_{scat}^c	χ_{ν}^2 (dof)
Mrk 348 ^d	13.2	1.56	10.4	6.42	40	54	3.16	6.26	2.18(150)
3C 33 ^d	35.4	1.33	0.931	6.44	100	260	2.17	3.17	1.52(42)
2MASX J02281350–0315023	$20.6^{+14.6}_{-3.5}$	1.9(f)	$0.75^{+0.14}_{-0.12}$	$6.40^{+0.040}_{-0.040}$	$0(<60)$	$170(<360)$	$0.41(<0.84)$	$0.35^{+0.17}_{-0.17}$	0.72(14)
NGC 1142	$63.9^{+3.2}_{-3.2}$	$2.32^{+0.06}_{-0.12}$	$16.20^{+0.28}_{-0.28}$	$6.410^{+0.040}_{-0.040}$	$0(<60)$	180^{+60}_{-50}	$4.0^{+1.3}_{-1.3}$	$4.32^{+0.33}_{-0.33}$	1.32(92)
3C 98	$14.43^{+0.98}_{-0.89}$	$1.900^{+0.065}_{-0.069}$	$1.889^{+0.068}_{-0.068}$	6.40(f)	10(f)	63^{+49}_{-49}	$0.36^{+0.28}_{-0.28}$	$2.23^{+0.26}_{-0.26}$	1.17(143)
B2 0857+39	$19.0^{+3.5}_{-3.9}$	1.9(f)	$0.41^{+0.10}_{-0.09}$	6.40(f)	10(f)	$42(<240)$	$0.06(<0.36)$	$0.25^{+0.16}_{-0.16}$	1.16(15)
IC 2461	$7.05^{+0.20}_{-0.20}$	$1.728^{+0.055}_{-0.053}$	$1.400^{+0.037}_{-0.042}$	$6.409^{+0.036}_{-0.035}$	106^{+49}_{-36}	210^{+54}_{-48}	$1.21^{+0.31}_{-0.27}$	$0.323^{+0.065}_{-0.064}$	0.96(118)
2MASX J10335255+0044033	$19.5^{+5.9}_{-4.2}$	1.9(f)	$0.52^{+0.13}_{-0.10}$	6.40(f)	10(f)	$0(<105)$	$0(<0.18)$	$0.73^{+0.20}_{-0.27}$	0.83(8)
MCG +08–21–065	$23.6^{+3.9}_{-3.2}$	1.9(f)	$0.81^{+0.14}_{-0.12}$	6.40(f)	10(f)	190^{+140}_{-140}	$0.46^{+0.34}_{-0.35}$	$0.21^{+0.16}_{-0.16}$	0.76(23)
NGC 4074	$19.2^{+4.4}_{-3.5}$	1.9(f)	$2.27^{+0.58}_{-0.46}$	6.40(f)	10(f)	$190(<430)$	$1.3(<2.9)$	$3.12^{+0.73}_{-0.73}$	0.98(13)
NGC 4138	$7.66^{+0.45}_{-0.40}$	$1.592^{+0.058}_{-0.059}$	$1.769^{+0.051}_{-0.054}$	$6.380^{+0.061}_{-0.040}$	10(f)	85^{+55}_{-45}	$0.82^{+0.43}_{-0.45}$	$1.75^{+0.24}_{-0.22}$	1.11(180)
NGC 4388 ^d	32.8	1.88	23.0	6.43	38	170	12.1	11.7	2.18(162)
NGC 4507 ^d	52.6	2.44	62.3	6.41	0	120	8.06	20.8	5.12(210)
ESO 506–G027 ^d	$66.0^{+5.0}_{-4.1}$	$1.280^{+0.072}_{-0.075}$	$2.67^{+0.13}_{-0.14}$	$6.412^{+0.026}_{-0.022}$	53^{+31}_{-36}	350^{+120}_{-70}	$8.9^{+2.0}_{-1.8}$	$1.30^{+0.17}_{-0.18}$	1.17(80)
2MASX J12544196–3019224	$20.6^{+4.8}_{-5.3}$	1.9(f)	$0.45^{+0.12}_{-0.12}$	6.40(f)	10(f)	$130(<410)$	$0.18(<0.57)$	$0.63^{+0.25}_{-0.25}$	$743.7(1923)^e$
NGC 4939	$19.3^{+3.3}_{-2.6}$	1.9(f)	$3.08^{+0.52}_{-0.45}$	6.40(f)	10(f)	$83(<220)$	$0.76(<2.01)$	$3.86^{+0.66}_{-0.67}$	1.21(28)
ESO 383–G18	$19.46^{+0.92}_{-0.86}$	$1.545^{+0.048}_{-0.046}$	$2.597^{+0.069}_{-0.067}$	$6.325^{+0.054}_{-0.054}$	100^{+76}_{-71}	130^{+40}_{-53}	$1.95^{+0.69}_{-0.77}$	$2.68^{+0.21}_{-0.23}$	1.30(134)
ESO 103–G035	$18.99^{+0.48}_{-0.46}$	$1.775^{+0.040}_{-0.039}$	$15.79^{+0.24}_{-0.23}$	$6.476^{+0.023}_{-0.022}$	$3(<47)$	67 ± 19	3.9 ± 1.1	$3.03^{+0.34}_{-0.32}$	1.19(136)
IC 4995 ^d	59.6	3.44	11.1	6.40	0	790	1.50	2.80	1.93(19)
NGC 7070A	$12.4^{+0.7}_{-1.1}$	$1.510^{+0.070}_{-0.069}$	$0.72^{+0.22}_{-0.19}$	6.40(f)	10(f)	$38(<77)$	$0.17(<0.34)$	0.669 ± 0.090	0.98(96)
NGC 7172	$7.810^{+0.072}_{-0.070}$	$1.656^{+0.013}_{-0.015}$	15.56 ± 0.09	$6.380^{+0.021}_{-0.019}$	80 ± 25	71^{+11}_{-9}	$5.20^{+0.80}_{-0.70}$	3.62 ± 0.24	1.30(173)
NGC 7319 ^d	66.1	2.25	6.14	6.39	48	250	2.39	2.81	2.99(131)

NOTE. — Photon index of the power law with only Galactic absorption was assumed to be the same value as power law absorbed by cold matter at the redshift of the source. (f) indicates fixed the parameter.

^a Normalization of the absorbed power law in units of $10^{-3} \text{ photons cm}^{-2} \text{ s}^{-1}$ at 1 keV.

^b Normalization of the Gaussian line in units of $10^{-5} \text{ photons cm}^{-2} \text{ s}^{-1}$ in the line.

^c Normalization of the less absorbed power law in units of $10^{-5} \text{ photons cm}^{-2} \text{ s}^{-1}$ at 1 keV.

^d Errors were not calculated for the case of χ_{ν}^2 exceeding 1.5.

^e C-statistic was used to fit the unbinned spectrum. C-statistics and number of bins (in parenthesis) are shown.

TABLE 3
SPECTRAL PARAMETERS FOR ABSORPTION, POWER LAW, AND GAUSSIAN IN THE COMPLEX MODELS

Name	N_{H} (10^{22} cm^{-2})	Γ	A_{int}^a	E_{line} (keV)	σ (eV)	Fe EW (eV)	A_{ga}^b	A_{scat}^c	χ_{ν}^2 (dof)
Mrk 348	$19.07^{+0.56}_{-0.52}$	$1.677^{+0.021}_{-0.018}$	$11.89^{+0.20}_{-0.21}$	$6.448^{+0.026}_{-0.032}$	$5(<69)$	52^{+18}_{-12}	$2.60^{+0.86}_{-0.68}$	$3.41^{+0.46}_{-0.31}$	1.10(137)
3C 33	77^{+22}_{-16}	$2.03^{+0.23}_{-0.25}$	$6.3^{+0.9}_{-2.7}$	$6.41^{+0.10}_{-0.07}$	$55(<149)$	180 ± 120	2.8 ± 1.8	$1.22^{+0.56}_{-0.62}$	1.13(40)
NGC 1142	$56.5^{+3.2}_{-3.6}$	$1.815^{+0.037}_{-0.073}$	5.19 ± 0.26	6.414 ± 0.028	$20(<69)$	220 ± 60	3.8 ± 1.2	2.84 ± 0.31	1.16(90)
3C 98	$12.5^{+1.3}_{-0.8}$	$1.64^{+0.07}_{-0.10}$	$1.11^{+0.24}_{-0.27}$	6.4(f)	0(f)	65 ± 50	0.36 ± 0.27	$1.20^{+0.39}_{-0.28}$	1.01(142)
IC 2461	$6.84^{+0.20}_{-0.18}$	$1.691^{+0.028}_{-0.031}$	$1.305^{+0.028}_{-0.025}$	6.409 ± 0.034	105^{+47}_{-36}	211^{+47}_{-49}	$1.20^{+0.27}_{-0.28}$	$0.18^{+0.10}_{-0.11}$	0.88(116)
NGC 4138	$7.60^{+0.40}_{-0.38}$	$1.492^{+0.035}_{-0.037}$	$1.460^{+0.040}_{-0.045}$	$6.380^{+0.089}_{-0.041}$	10(f)	86^{+44}_{-37}	$0.79^{+0.44}_{-0.33}$	$1.17^{+0.24}_{-0.24}$	1.03(178)
NGC 4388	$29.1^{+2.1}_{-1.1}$	$1.479^{+0.036}_{-0.035}$	$8.59^{+0.16}_{-0.17}$	6.431 ± 0.016	$42(<68)$	220 ± 30	$12.0^{+2.0}_{-1.8}$	$4.67^{+0.71}_{-0.65}$	1.10(157)
NGC 4507	$42.84^{+0.81}_{-0.78}$	1.500 ± 0.012	$7.050^{+0.079}_{-0.088}$	6.419 ± 0.013	$5(<34)$	120 ± 16	$5.80^{+0.77}_{-0.74}$	9.81 ± 0.32	1.17(199)
ESO 506–G027	117^{+11}_{-11}	$1.557^{+0.072}_{-0.093}$	$6.8^{+0.3}_{-0.3}$	$6.408^{+0.024}_{-0.022}$	51^{+30}_{-40}	520^{+130}_{-170}	$20.5^{+5.1}_{-6.6}$	1.25 ± 0.19	0.93(79)
NGC 4939	$18.6^{+2.9}_{-2.4}$	1.9(f)	$3.03^{+0.51}_{-0.45}$	6.4(f)	10(f)	$87(<220)$	$0.84(<2.02)$	$2.85^{+0.69}_{-0.77}$	1.08(27)
ESO 383–G18	$18.75^{+0.98}_{-0.96}$	$1.440^{+0.063}_{-0.064}$	$1.88^{+0.09}_{-0.09}$	6.4(f)	$30(<130)$	100^{+50}_{-40}	$1.34^{+0.62}_{-0.55}$	$1.47^{+0.24}_{-0.27}$	1.11(133)
ESO 103–G035	$20.60^{+0.57}_{-0.56}$	$1.922^{+0.039}_{-0.041}$	$19.14^{+0.28}_{-0.29}$	6.475 ± 0.026	$3(<43)$	66^{+22}_{-19}	3.6 ± 1.1	$1.30^{+0.55}_{-0.55}$	1.02(133)
IC 4995	45^{+21}_{-9}	1.9(f)	$0.45^{+0.12}_{-0.16}$	6.390 $^{+0.057}_{-0.036}$	$0(<66)$	890^{+420}_{-440}	$1.20^{+0.56}_{-0.59}$	$0.90^{+0.32}_{-0.33}$	1.14(15)
NGC 7172	7.872 ± 0.071	1.661 ± 0.014	15.78 ± 0.09	6.380 ± 0.020	72^{+28}_{-24}	69 ± 11	5.10 ± 0.74	$2.81^{+0.24}_{-0.33}$	1.18(168)
NGC 7319	$75.5^{+6.2}_{-5.7}$	$1.90^{+0.12}_{-0.26}$	$2.70^{+0.11}_{-0.87}$	6.392 ± 0.023	$54(<97)$	370 ± 80	$3.00^{+0.65}_{-0.62}$	1.25 ± 0.20	1.13(128)

NOTE. — Photon index of the power law with only Galactic absorption was assumed to be the same value as the hard power law absorbed by cold matter at the redshift of the source. (f) indicates fixed parameter.

^a Normalization of the absorbed power law in units of $10^{-3} \text{ photons cm}^{-2} \text{ s}^{-1}$ at 1 keV.

^b Normalization of the Gaussian line in units of $10^{-5} \text{ photons cm}^{-2} \text{ s}^{-1}$ in the line.

^c Normalization of the less absorbed power law in units of $10^{-5} \text{ photons cm}^{-2} \text{ s}^{-1}$ at 1 keV.

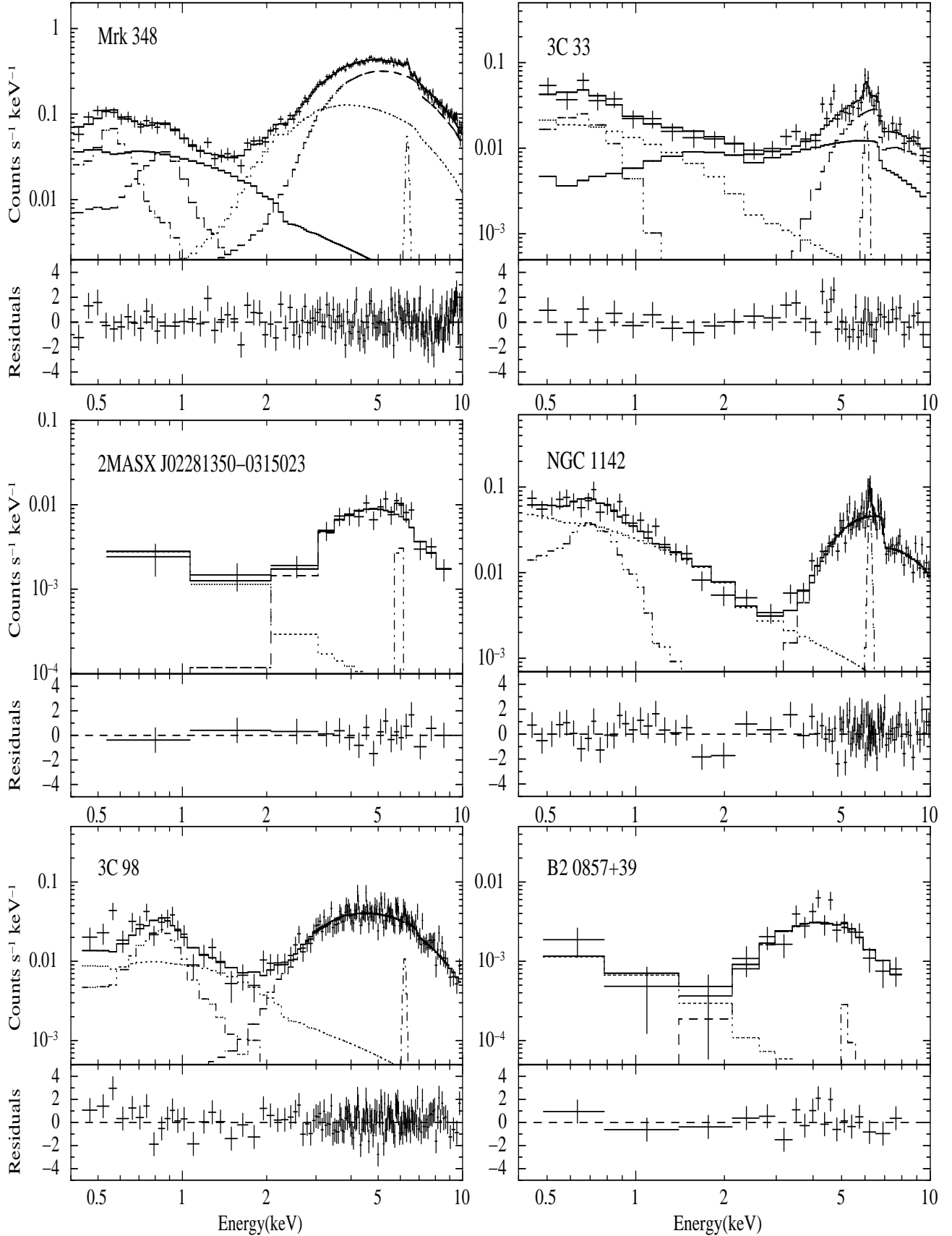


FIG. 2.— X-ray spectra (upper panels) and residuals in units of σ (or data/model ratio; lower panels). Model components are shown with dashed, dotted, dot-dashed, and dot-dot-dot-dashed lines. Although an unbinned spectrum was used in the fit of 2MASX J12544196-3019224, a binned spectrum is shown for the presentation purpose.

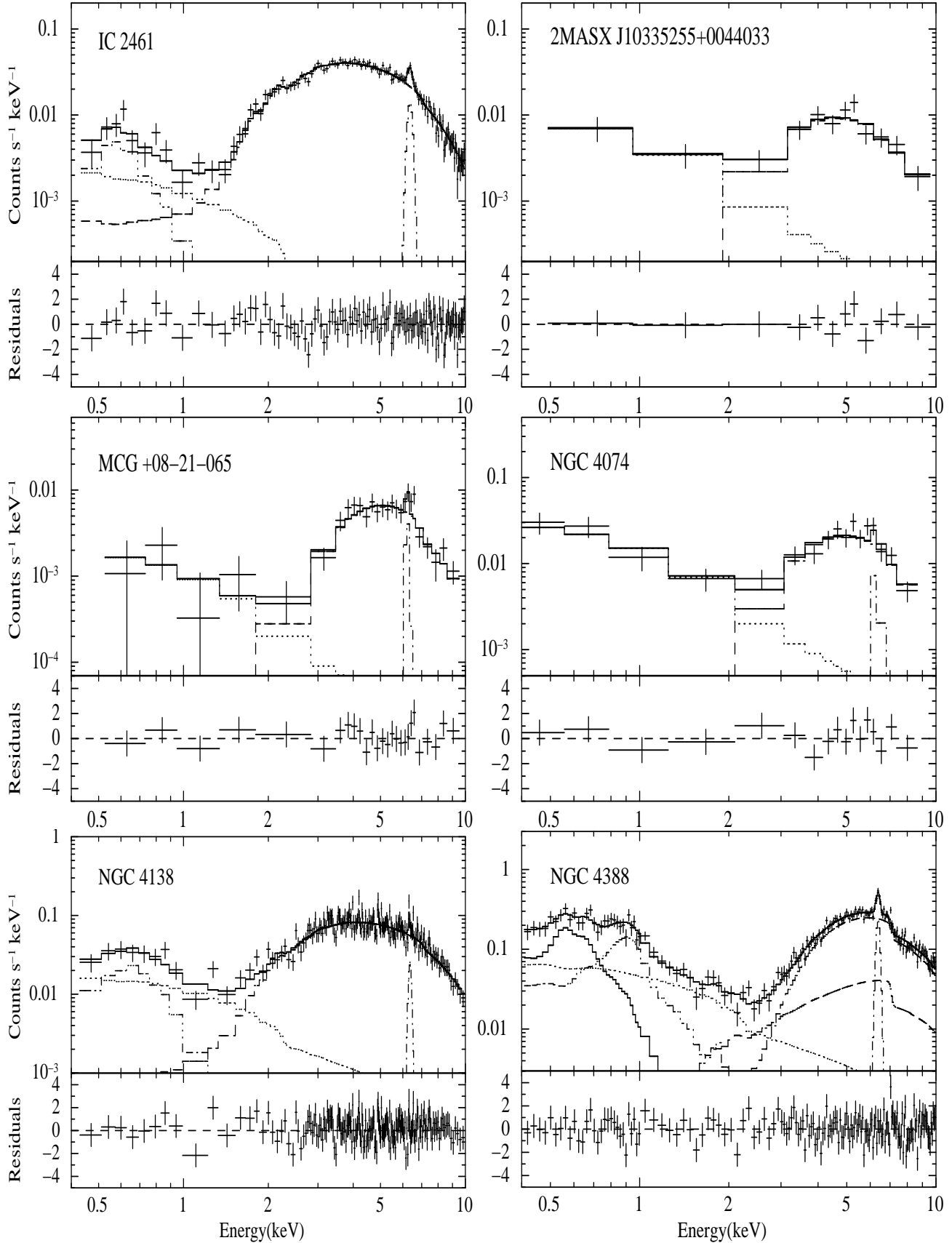


FIG. 2.— Continued

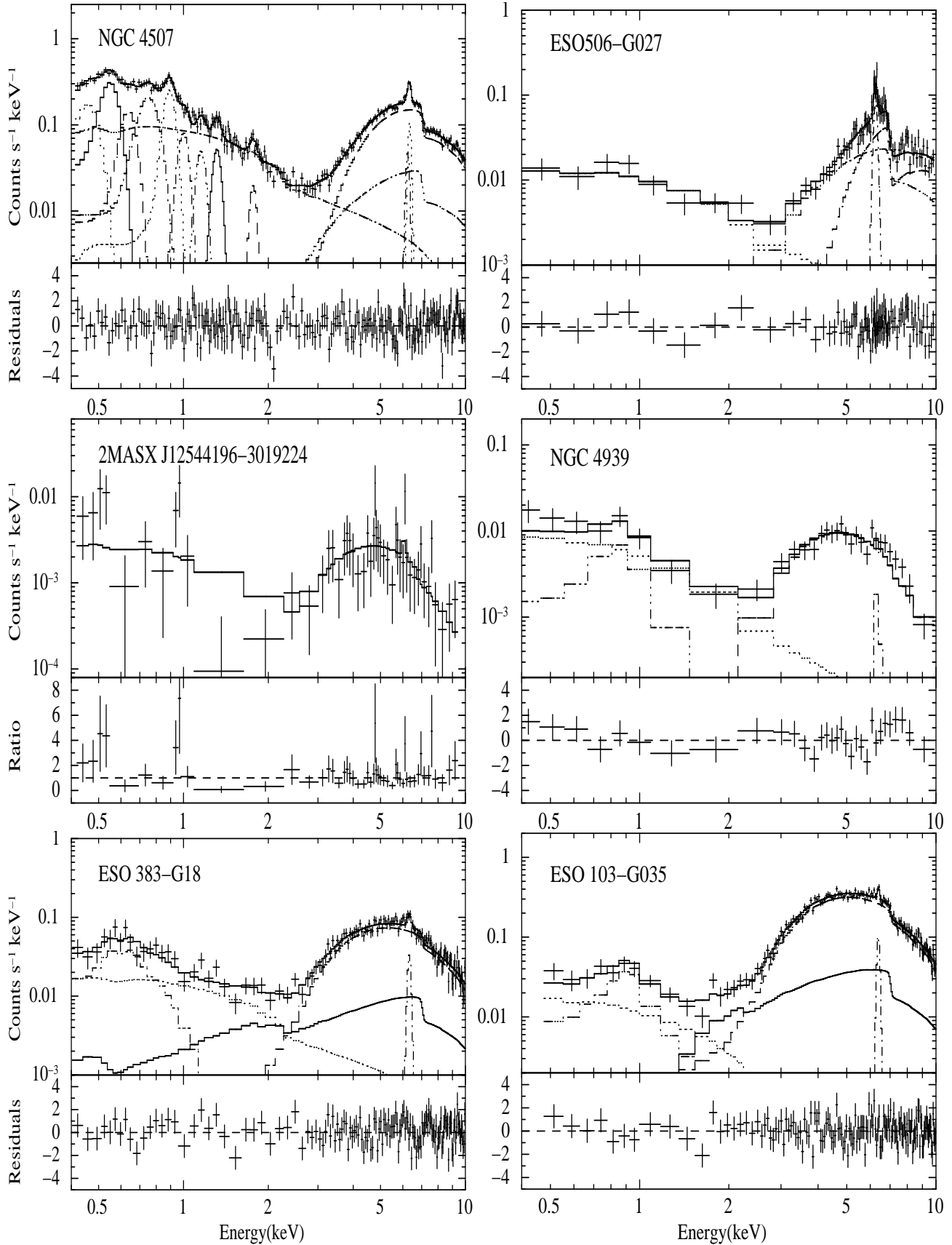


FIG. 2.— Continued

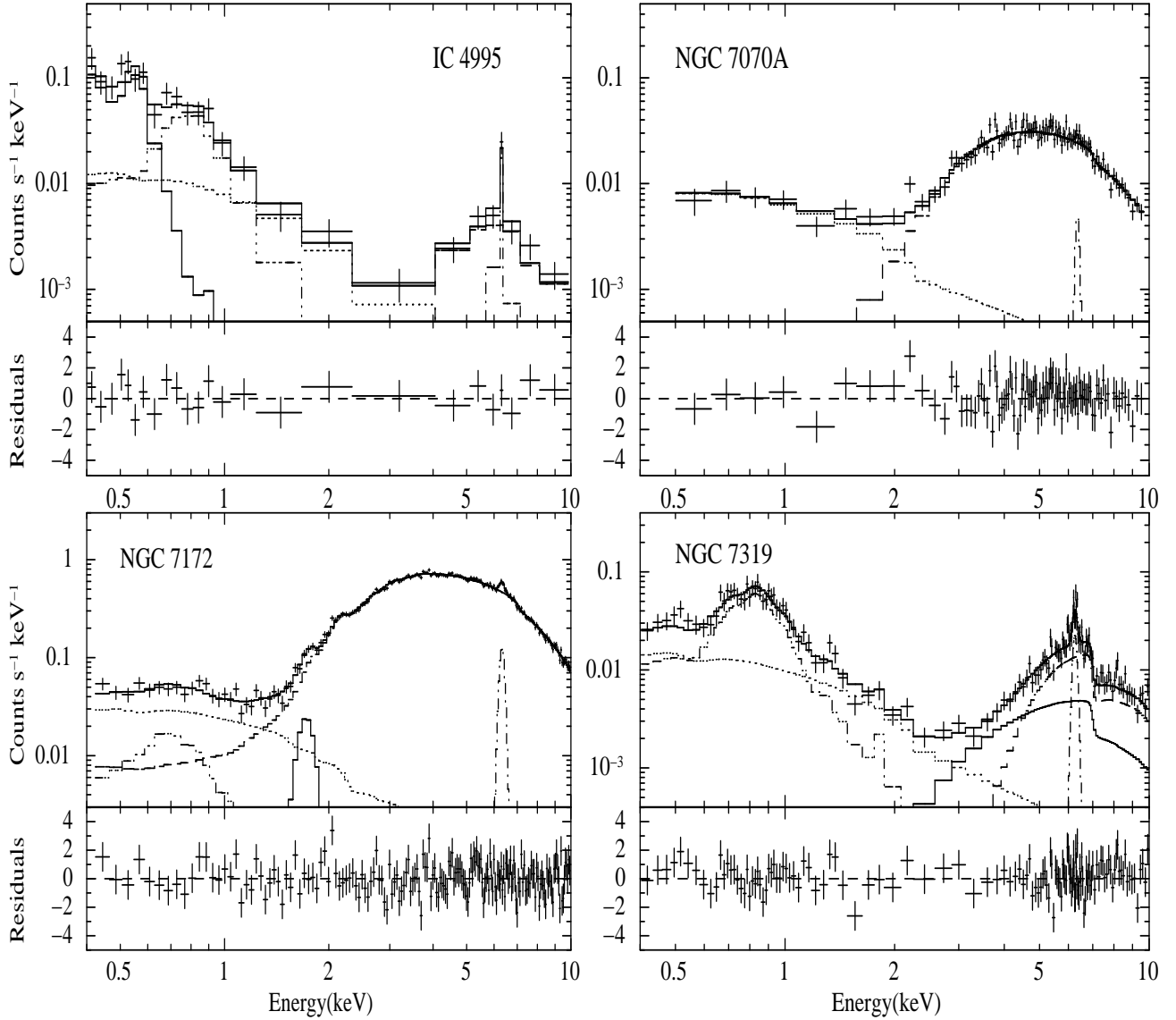


FIG. 2.— Continued

in the ionized gas. High-resolution spectra of some Seyfert 2 galaxies obtained with *Chandra* or *XMM-Newton* have shown that emission from a photoionized or photoexcited plasma is dominant in soft X-rays (e.g., Sako et al. 2000; Kinkhabwala et al. 2002). Another possibility is the contribution of thermal emission from a collisionally ionized plasma, which is heated by shocks induced by AGN outflows (King 2005) or intense star formation. For example, a high-resolution image of NGC 4945 with *Chandra* suggested that the soft X-rays are mostly dominated by thermal radiation from a starburst region (Schurch et al. 2002).

Far-infrared (FIR) luminosities are often used to estimate the contribution of starburst since star-forming activity is much more effective than the AGN in powering the FIR emission. A tight linear relation between the soft X-ray and the FIR luminosity is known for starburst and normal galaxies (e.g., David et al. 1992; Ranalli et al. 2003). Thus, the FIR luminosity can be used to determine the contribution of starburst to the soft X-ray. The FIR luminosities of our sample were calculated using the formula defined in Helou et al. (1985), based on flux densities at 60 μ m and 100 μ m. In-

frared fluxes (60 μ m and 100 μ m) measured with *Infrared Astronomical Satellite (IRAS)* for 12 objects were taken from the NED. *IRAS* fluxes for the rest of the 10 objects are not available. The soft X-ray luminosities were calculated from fluxes in 0.5–2 keV corrected for absorption given in Table 7, Columns 9 and 11, except for NGC 4507 and NGC 7172. For calculations of the soft X-ray luminosities of NGC 4507 and NGC 7172, absorption corrected fluxes of the Gaussians in 0.5–2 keV (NGC 4507: 27.6×10^{-14} erg cm $^{-2}$ s $^{-1}$, NGC 7172: 1.53×10^{-14} erg cm $^{-2}$ s $^{-1}$), were added to the fluxes given in Table 7, Columns 9 and 11. The calculated FIR and soft X-ray luminosities are shown in Table 8 and the relation between the soft X-ray and the FIR luminosity for our sample is shown in Figure 3. The area surrounded by two solid lines expresses the region for starburst galaxies in Ranalli et al. (2003). About a half of our sample is in the starburst region. This means that the contribution from starburst is likely to be large in the soft X-ray emission of these sources. Therefore, it should be noted that starburst contribution may not be negligible in the soft X-ray emission in calculating scattering fractions in section 4.2 for about a half of our sample. If starburst significantly

TABLE 4
SPECTRAL PARAMETERS FOR MEKAL AND THE THIRD POWER LAW IN THE COMPLEX MODELS

Name	MEKAL ^a		MEKAL ^a		Power law	
	<i>kT</i> (keV)	<i>A_m</i> ^b	<i>kT</i> (keV)	<i>A_m</i> ^b	<i>N_H</i> ^c (10 ²² cm ⁻²)	<i>A</i> ^d
Mrk 348	0.68 ^{+0.13} _{-0.09}	2.04 ^{±0.38}	0.169 ^{+0.015} _{-0.013}	6.0 ^{±1.0}	7.48 ^{±0.20}	2.78 ^{±0.14}
3C 33	0.29 ^{+0.10} _{-0.07}	2.07 ^{+0.91}
NGC 1142	0.295 ^{+0.033} _{-0.043}	3.70 ^{+0.70} _{-0.72}
3C 98	0.65(f)	1.69 ^{+0.34} _{-0.43}
IC 2461	0.211 ^{+0.054} _{-0.049}	0.39 ^{+0.17} _{-0.15}
NGC 4138	0.265 ^{+0.062} _{-0.048}	1.44 ^{±0.42}
NGC 4388	0.78 ^{+0.11} _{-0.10}	7.60 ^{+0.89} _{-0.93}	0.203 ^{+0.056} _{-0.014}	10.9 ^{+0.7} _{-1.6}	2.5 ^{+1.4} _{-1.0}	...
NGC 4507	9.1 ^{+3.0} _{-2.5}	...
ESO 506-G027	12.5 ^{+3.0} _{-2.5}	...
NGC 4939	0.65(f)	1.9 ^{+1.0} _{-1.2}
ESO 383-G18	0.232 ^{+0.030} _{-0.036}	2.77 ^{+0.63} _{-0.57}
ESO 103-G035	0.81 ^{+0.16} _{-0.11}	2.27 ^{+0.50} _{-0.48}	2.42 ^{+0.73} _{-0.49}	...
IC 4995	0.52 ^{+0.12} _{-0.14}	2.40 ^{+0.55} _{-0.57}	0.081(<0.085)	113 ⁺²¹ ₋₂₄
NGC 7172	0.302 ^{+0.073} _{-0.061}	1.30 ^{±0.37}
NGC 7319	0.621 ^{+0.034} _{-0.037}	3.51 ^{±0.36}	7.7 ^{+2.8} _{-2.2}	...

NOTE. — (f) indicates the fixed parameter.

^a Metal abundances were fixed at 0.5 solar.

^b Normalization of mekal in units of 10⁻¹⁹/(4π(*D_A* × (1+z))²) ∫ *n_e* *n_H* d*V*, where *D_A* is the angular size distance to the source (cm), *n_e* is the electron density (cm⁻³), and *n_H* is the hydrogen density (cm⁻³).

^c Absorption of pexrav or the third power law by cold matter at the redshift of the source.

^d Normalization of the third power law in units of 10⁻³ photons cm⁻² s⁻¹ at 1 keV.

TABLE 5
SPECTRAL PARAMETERS FOR GAUSSIANS IN THE COMPLEX MODELS

Name	<i>E_{line}</i> (keV)	σ (eV)	<i>A_{ga}</i> ^a	Identification
Mrk 348.....	6.670 ^{±0.045}	60(<111)	-2.52 ^{+0.72} _{-0.60}	Fe XXV
	7.000 ^{+0.035} _{-0.032}	0(<67)	-1.74 ^{+0.59} _{-0.54}	Fe XXVI
NGC 7172.....	1.734 ^{+0.046} _{-0.041}	77 ⁺⁵¹ ₋₃₆	0.57 ^{±0.20}	Si K α
NGC 4507.....	0.475 ^{±0.007}	10(f)	6.50 ^{+0.78} _{-0.75}	O VII K α
	0.560 ^{+0.003} _{-0.004}	10(f)	11.00 ^{+0.79} _{-0.76}	O VII K α
	0.648 ^{±0.007}	10(f)	3.15 ^{+0.42} _{-0.40}	O VIII K α
	0.758 ^{±0.006}	46 ⁺⁷ ₋₆	5.04 ^{±0.37}	O VII RRC
	0.904 ^{±0.005}	10(f)	3.31 ^{+0.26} _{-0.24}	Ne IX K α
	1.013 ^{+0.014} _{-0.013}	10(f)	0.93 ^{±0.17}	Ne X K α
	1.169 ^{+0.016} _{-0.018}	10(f)	0.52 ^{±0.12}	Fe XXIII L
	1.330 ^{+0.012} _{-0.013}	10(f)	0.53 ^{+0.09} _{-0.13}	Mg XI K α
	1.788 ^{+0.033} _{-0.026}	10(f)	0.204 ^{±0.085}	Si XIII K α
	6.320(f)	40(f)	3.05 ^{+0.79} _{-0.77}	Fe I–XVI CS ^b

NOTE. — (f) indicates fixed the parameter.

^a Normalization of the Gaussian line in units of 10⁻⁵ photons cm⁻² s⁻¹.

^b Compton shoulder.

contributes to the soft X-ray emission, the level of scattered emission would be much lower than those derived in Section 4.2.

4.2. Scattering Fraction

Scattering fractions are often calculated with the following equation;

$$f_{\text{scat}} = \frac{A_{\text{scat}}}{A_{\text{int}}},$$

where *A_{int}* and *A_{scat}* are the normalization for the power law with large and only Galactic absorption, respectively. The values calculated for our sample are shown in Table 9. Since the

TABLE 6
BEST-FIT MODELS FOR OUR SAMPLE

Name	Model ^a
Mrk 348	BM + two MEKAL + two lines + abs-PL
3C 33	BM + MEKAL + Ref
2MASX J02281350–0315023	BM
NGC 1142	BM + MEKAL
3C 98	BM + MEKAL
B2 0857+39	BM
IC 2461	BM + MEKAL
2MASX J10332555+0044033	BM
MCG +08-21-065	BM
NGC 4074	BM
NGC 4138	BM + MEKAL
NGC 4388	BM + two MEKAL + abs-Ref
NGC 4507	BM + ten lines + abs-Ref
ESO 506-G027	BM + abs-Ref
2MASX J12544196–3019224	BM
NGC 4939	BM + MEKAL
ESO 383-G18	BM + MEKAL + Ref
ESO 103-G035	BM + MEKAL + abs-Ref
IC 4995	BM + two MEKAL
NGC 7070A	BM
NGC 7172	BM + MEKAL + line
NGC 7319	BM + MEKAL + abs-Ref

^a BM: Baseline model, PL: power law, MEKAL: thin thermal plasma model (mekal), Ref: cold refection model (pexrav), abs-PL(or Ref): absorbed PL(or Ref). All components are absorbed by the Galactic absorption.

origin of soft X-ray emission is not clear as discussed in Section 4.1, we calculated scattering fractions with the equation as follows;

$$f_{\text{scat}}^{\text{obs}} = \frac{F_{0.5-2}^{\text{soft}}}{F_{0.5-2}^{\text{int}}},$$

where *F_{0.5-2}^{int}* and *F_{0.5-2}^{soft}* are absorption corrected fluxes in the 0.5–2 keV band for the power law corresponding to the direct emission and all the components except for the direct power law, respectively. This value is regarded as an upper limit on the scattering fraction. The obtained values (Table 9) except

TABLE 7
FLUX FOR THE BEST-FIT MODEL

Name (1)	Total		Power Law _{total}				Power Law _{scat}		MEKAL	
	(Observed) 0.5–2 keV (2)	(Observed) 2–10 keV (3)	(Observed) 0.5–2 keV (4)	(Observed) 2–10 keV (5)	(Intrinsic) 0.5–2 keV (6)	(Intrinsic) 2–10 keV (7)	(Observed) 0.5–2 keV (8)	(Intrinsic) 0.5–2 keV (9)	(Observed) 0.5–2 keV (10)	(Intrinsic) 0.5–2 keV (11)
Mrk 348	12.3	27.9	8.36	28.1	32.2	60.9	6.33	7.49	3.97	5.50
3C 33	6.06	2.51	2.16	1.56	12.4	13.8	2.16	2.41	1.41	1.69
2MASX J02281350–0315023	0.637	0.817	0.637	0.792	1.44	1.94	0.634	0.681
NGC 1142	7.49	3.11	5.04	2.97	11.1	17.0	5.03	6.01	2.45	3.35
3C 98	3.49	2.62	2.02	2.59	2.40	4.82	1.94	2.57	1.47	2.14
B2 0857+39	0.376	0.420	0.376	0.417	0.624	0.841	0.353	0.377
IC 2461	1.92	3.55	1.67	3.44	2.89	5.35	0.383	0.396	0.254	0.273
2MASX J10335255+0044033	1.10	0.557	1.10	0.557	0.918	1.24	1.10	1.28
MCG +08-21-065	0.415	0.843	0.415	0.814	1.71	2.21	0.414	0.439
NGC 4074	6.17	2.75	6.17	2.66	4.90	6.61	6.16	6.64
NGC 4138	4.77	5.44	3.58	5.37	3.32	8.30	2.56	2.65	1.19	1.28
NGC 4388	25.2	20.7	9.73	17.1	19.4	49.4	9.73	10.5	14.9	16.9
NGC 4507	36.6	12.5	18.1	10.2	15.9	39.1	18.1	21.9
ESO 506-G027	2.30	4.06	2.30	2.22	15.1	34.2	2.30	2.68
2MASX J12544196–3019224	1.05	0.527	1.05	0.491	0.906	1.22	1.05	1.27
NGC 4939	7.79	3.65	5.60	3.59	6.66	8.98	5.60	6.22	2.19	2.47
ESO 383-G18	5.42	6.09	2.94	5.25	4.24	11.5	2.94	3.28	1.66	2.14
ESO 103-G035	5.72	23.2	2.37	20.1	41.5	54.3	2.35	2.82	2.40	2.90
IC 4995	6.29	0.348	1.71	0.295	0.992	1.34	1.71	1.94	4.59	5.92
NGC 7070A	1.43	2.17	1.43	2.16	1.63	3.99	1.39	1.50
NGC 7172	17.5	42.3	14.8	41.8	34.9	67.6	5.85	6.21	1.13	1.25
NGC 7319	5.80	1.34	2.16	0.905	5.78	7.82	2.16	2.61	3.62	4.56

NOTE. — The units of Columns 2, 4, 8, 9, 10, and 11 are 10^{-14} erg cm $^{-2}$ s $^{-1}$. The units of Columns 3, 5, 6, and 7 are 10^{-12} erg cm $^{-2}$ s $^{-1}$.

TABLE 8
HARD X-RAY, SOFT X-RAY, FAR INFRARED, AND [O III] λ 5007 LUMINOSITIES

Name (1)	Hard (2)	Soft (3)	FIR (4)	[O III] (5)	Reference (6)
Mrk 348	43.49	40.82	43.49	41.95	1
3C 33	44.07	41.55	...	42.52	2
2MASX J02281350–0315023	43.46	41.01
NGC 1142	43.51	41.25	44.77	41.87	3
3C 98	43.01	41.00	...	41.91	4
B2 0857+39	44.12	41.77
IC 2461	41.83	38.93	43.00
2MASX J10335255+0044033	43.75	41.77	...	43.62	5
MCG +08-21-065	42.65	39.95	43.51	39.78	6
NGC 4074	42.88	40.88	...	42.05	7
NGC 4138	41.21	38.88	...	38.75	8
NGC 4388	42.89	40.63	43.94	41.77	1
NGC 4507	43.09	41.19	43.81	41.69	1
ESO 506-G027	43.69	40.58	43.58	42.96	9
2MASX J12544196–3019224	42.96	40.98
NGC 4939	42.33	40.31	43.59	41.43	1
ESO 383-G18	42.60	40.27
ESO 103-G035	43.33	40.35	43.54	41.65	1
IC 4995	41.88	40.66	43.40	41.96	7
NGC 7070A	41.75	39.33	42.40
NGC 7172	43.06	40.18	43.77	39.83	1
NGC 7319	42.95	40.92	...	41.44	1

REFERENCES. — (1) Bassani et al. 1999; (2) Yee & Oke 1978; (3) Shu et al. 2007; (4) Costero & Osterbrock 1977; (5) Dong et al. 2005; (6) Line flux measurement based on the Sloan Digital Sky Survey data at MPA/JHU (<http://www.mpa-garching.mpg.de/SDSS/>); Kauffmann et al. 2003; (7) Polletta et al. 1996; (8) Ho et al. 1997; (9) Landi et al. 2007.

NOTE. — Column 1: Galaxy name. Column 2: Logarithm of intrinsic 2–10 keV luminosity. Column 3: Logarithm of intrinsic 0.5–2 keV luminosity of soft X-ray components. Column 4: Logarithm of far-infrared luminosity. Column 5: Logarithm of reddening corrected [O III] luminosity. Column 6: References for [O III] luminosity.

for NGC 4507 and IC 4995 are smaller than the value typical for other Seyfert 2s observed so far, which is about 3% (e.g., Turner et al. 1997; Bianchi and Guainazzi 2007). In partic-

ular, those of eight sources are less than 0.5%. These are in the range recently found by hard X-ray surveys (Ueda et al. 2007; Winter et al. 2008).

The scattering fraction can be related to the geometry of the scatterer;

$$f_{\text{scat}} \sim \tau \frac{\Delta\Omega}{4\pi},$$

where $\Delta\Omega$ and τ are the solid angle subtended by the scattering electrons and a scattering optical depth, respectively. Thus, the small scattering fraction indicates that $\Delta\Omega$ and/or τ are small. If τ does not differ much from object to object, our sample with a small scattering fraction is strong candidates for AGNs buried in a very geometrically thick torus with a small opening angle.

4.3. Comparison with [O III] λ 5007 luminosity

[O III] λ 5007 emission is produced in the narrow line region (NLR), which is considered to exist in the opening direction of the torus. Since the X-ray scattering region is also spatially extended along the NLR (Sako et al. 2000; Young et al. 2001; Bianchi et al. 2006), we expect that an AGN buried in a geometrically thick torus with a small opening part should have a fainter [O III] emission luminosity relative to a hard X-ray luminosity compared with classical Seyfert 2 galaxies with a large opening part.

We collected [O III] luminosities for 16 objects in our sample from the literature as shown in Table 8. The [O III] fluxes were corrected for the extinction by using the relation

$$L_{[\text{O III}]}^{\text{int}} = L_{[\text{O III}]}^{\text{obs}} \left[\frac{\text{H}\alpha/\text{H}\beta}{(\text{H}\alpha/\text{H}\beta)_0} \right]^{2.94},$$

assuming an intrinsic Balmer decrement $(\text{H}\alpha/\text{H}\beta)_0 = 3.0$, where $L_{[\text{O III}]}^{\text{obs}}$ and $\text{H}\alpha/\text{H}\beta$ are an observed [O III] luminosity

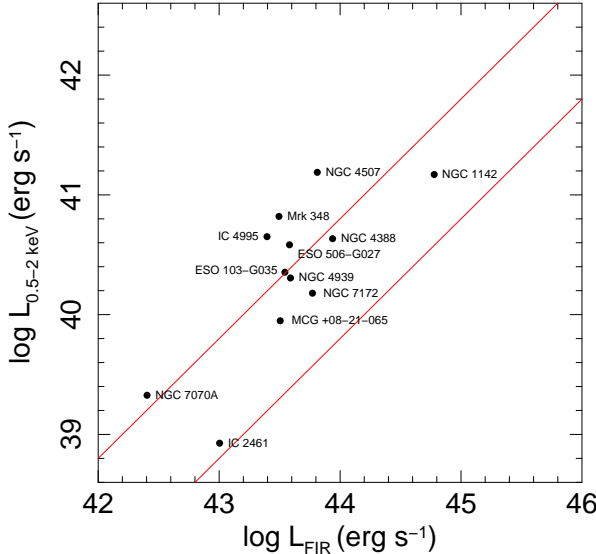


FIG. 3.— Comparison between intrinsic luminosity of the soft component in the 0.5–2 keV band and FIR luminosity. The area surrounded by two solid lines is a typical region for starburst galaxies (Ranalli et al. 2003).

TABLE 9
SCATTERING FRACTION

Name	f_{scat}^a (%)	$f_{\text{scat}}^{\text{obs}}b$ (%)
Mrk 348	0.29	0.40
3C 33	0.19	0.33
2MASX J02281350–0315023	0.47	0.47
NGC 1142	0.55	0.84
3C 98	1.1	2.0
B2 0857+39	0.61	0.61
IC 2461	0.14	0.23
2MASX J10335255+0044033	1.4	1.4
MCG +08-21-065	0.26	0.26
NGC 4074	1.4	1.4
NGC 4138	0.80	1.2
NGC 4388	0.54	1.4
NGC 4507	1.4	3.1
ESO 506-G027	0.18	0.18
2MASX J12544196–3019224	1.4	1.4
NGC 4939	0.94	1.3
ESO 383-G18	0.78	1.3
ESO 103-G035	0.068	0.14
IC 4995	2.0	8.1
NGC 7070A	0.93	0.93
NGC 7172	0.18	0.26
NGC 7319	0.46	1.3

^a Scattering fraction calculated by $f_{\text{scat}} = \frac{A_{\text{scat}}}{A_{\text{int}}}$, where A_{int} and A_{scat} are the normalization for the power law with large and only Galactic absorption, respectively.

^b Scattering fraction calculated by $f_{\text{scat}}^{\text{obs}} = \frac{F_{\text{soft}}^{\text{obs}}}{F_{0.5-2}^{\text{int}}}$, where $F_{0.5-2}^{\text{int}}$ and $F_{0.5-2}^{\text{soft}}$ are absorption corrected fluxes in the 0.5–2 keV band for the power law corresponding to the direct emission and all the components except for the direct power law, respectively.

and a ratio between observed $\text{H}\alpha$ and $\text{H}\beta$ line fluxes, respectively (Bassani et al. 1999).

Figure 4 shows the correlation between the intrinsic luminosities in the 2–10 keV band (L_{2-10}^{int}) and the reddening corrected [O III] line luminosities ($L_{[\text{O III}]}^{\text{int}}$) for our sample and a large sample of Seyfert 2 compiled by Bassani et al. (1999). From the latter sample, we used objects with N_{H} within $(0.6–20) \times 10^{23} \text{ cm}^{-2}$, which is the range observed for our sample. Some objects belong to both samples and such objects are regarded as members of our sample. The solid

lines in Figure 4 correspond to $L_{2-10}^{\text{int}}/L_{[\text{O III}]}^{\text{int}} = 1, 10, \text{ and } 100$ from bottom to top. The distribution of the $L_{2-10}^{\text{int}}/L_{[\text{O III}]}^{\text{int}}$ ratios for the two samples is shown in Figure 5. The ratios for Bassani’s sample are in the range 1–100, while those for most sources in our sample are > 10 . In particular, the ratios for three sources (MCG+08-21-065, NGC 4138, and NGC 7172) are greater than 100.

Netzer et al. (2006) showed that the ratio $L_{2-10}^{\text{int}}/L_{[\text{O III}]}^{\text{int}}$ increases with L_{2-10}^{int} such that

$$\log \frac{L_{2-10}^{\text{int}}}{L_{[\text{O III}]}^{\text{int}}} = (0.38 \pm 0.09) \log L_{2-10}^{\text{int}} - (15.0 \pm 4.0),$$

using a sample obtained from Bassani et al. (1999) and supplemented by Turner et al. (1997). Therefore, we compared the distribution of L_{2-10}^{int} between Bassani’s and our samples to examine whether the larger $L_{2-10}^{\text{int}}/L_{[\text{O III}]}^{\text{int}}$ in our sample is explained by this luminosity dependence. The distribution of L_{2-10}^{int} for Bassani’s and our samples is shown in Figure 6 as solid and dashed histograms, respectively. The distribution for our sample is slightly biased toward higher luminosities by $\log L_{2-10}^{\text{int}} \sim 0.5$. According to Netzer’s relation, this amount of shift in L_{2-10}^{int} results in an increase of $L_{2-10}^{\text{int}}/L_{[\text{O III}]}^{\text{int}}$ only by a factor of 1.5. We attempted the two-sample Kolmogorov–Smirnov test to examine the difference more quantitatively. The values of $L_{2-10}^{\text{int}}/L_{[\text{O III}]}^{\text{int}}$ were scaled to an assumed reference point $L_{2-10}^{\text{int}} = 10^{43} \text{ erg s}^{-1}$ by using Netzer’s relation, which was calculated by

$$\log \left[\frac{L_{2-10}^{\text{int}}}{L_{[\text{O III}]}^{\text{int}}} \right]_{\text{scaled}} = \log \frac{L_{2-10}^{\text{int}}}{L_{[\text{O III}]}^{\text{int}}} - 0.38 \log \left[\frac{L_{2-10}^{\text{int}}}{10^{43} \text{ erg s}^{-1}} \right].$$

The Kolmogorov–Smirnov test showed that the distributions of the scaled $L_{2-10}^{\text{int}}/L_{[\text{O III}]}^{\text{int}}$ for Bassani’s and our samples are drawn from the same parent population with the probability of 9.3%. Thus the difference of $L_{2-10}^{\text{int}}/L_{[\text{O III}]}^{\text{int}}$ between the two samples would not be explained solely by the luminosity dependence.

We found that [O III] luminosities for our sample are intrinsically lower than those of Seyfert 2s studied so far at a given X-ray luminosity, and agree with the above expectation. Although luminosities of optical narrow emission lines are often utilized as a good indicator of an intrinsic luminosity of an AGN and used for constructing the most unbiased samples (e.g., Mulchaey et al. 1994; Heckman 1995; Keel et al. 1994; Heckman et al. 2005), estimation of intrinsic luminosities of an AGN based on [O III] would have large uncertainties and surveys that rely on [O III] emission could be subject to biases against buried AGNs. In order to obtain complete unbiased samples of AGNs, hard X-ray surveys would be imperative.

5. CONCLUSION

We searched for AGNs, whose scattered emission is very weak, from the 2XMM Catalogue. In our selection procedure, we calculated HRs expected for an object with a small scattering fraction using a model consisting of absorbed and unabsorbed power laws and 22 sources were selected as candidates from the 2XMM Catalogue. Spectral analysis was conducted using the data observed with *XMM-Newton* for these 22 sources. Their X-ray spectra are represented by a combination of an absorbed power law with a column density of $\sim 10^{23-24} \text{ cm}^{-2}$, an unabsorbed power law, a narrow Gaussian

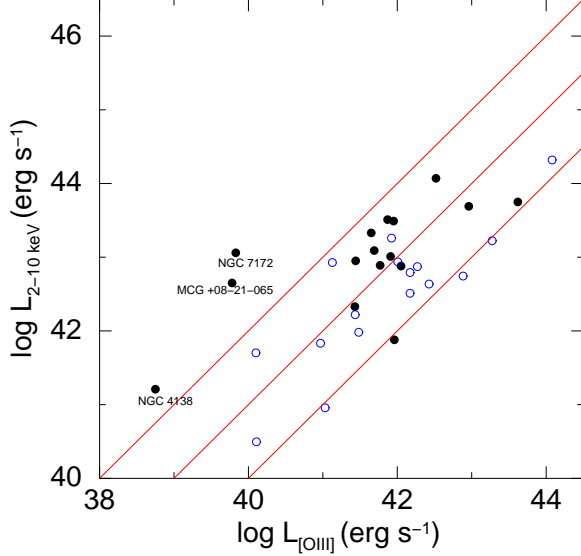


FIG. 4.— Comparison between intrinsic luminosity in the 2–10 keV band and reddening corrected [O III] line luminosity. Our sample is shown as filled circles. Other Seyfert 2s with N_{H} in the range of $(0.6\text{--}20)\times 10^{23} \text{ cm}^{-2}$ taken from Bassani et al. (1999) are shown as open circles. Solid lines correspond to $L_{\text{2-10 keV}}/L_{[\text{O III}]} = 1, 10, \text{ and } 100$ from bottom to top.

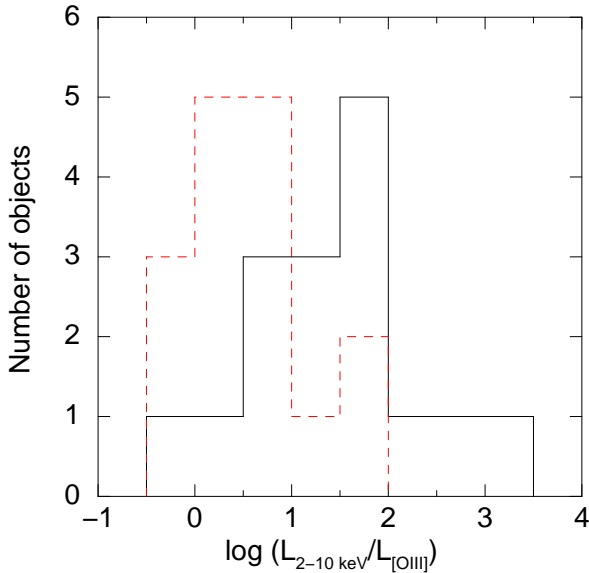


FIG. 5.— Distribution of the ratio between intrinsic luminosity in the 2–10 keV band and reddening corrected [O III] luminosity for our sample (solid histogram) and the Seyfert 2 sample compiled by Bassani et al. (1999) with N_{H} in the range of $(0.6\text{--}20)\times 10^{23} \text{ cm}^{-2}$ (dashed histogram).

line for the Fe K emission, and some additional components. The photon indices of the power-law components for 14 objects are in a typical range of Seyfert 2s ($\sim 1.5\text{--}2$). The photon indices for the others, which have large uncertainties in Γ , were fixed at 1.9 in our analysis. We found that the scattering fractions for our sample (except for NGC 4507 and IC 4995) were small compared to a typical value ($\sim 3\%$) of Seyfert 2s observed in the past. In addition, those of eight sources are less than 0.5%. If an opening angle of a torus is responsible for the scattering fraction, objects in our sample would be hidden by a geometrically thick torus with a small opening angle.

The ratios of $L_{0.5\text{--}2}^{\text{int}}/L_{\text{FIR}}$ for about a half of our sample are in

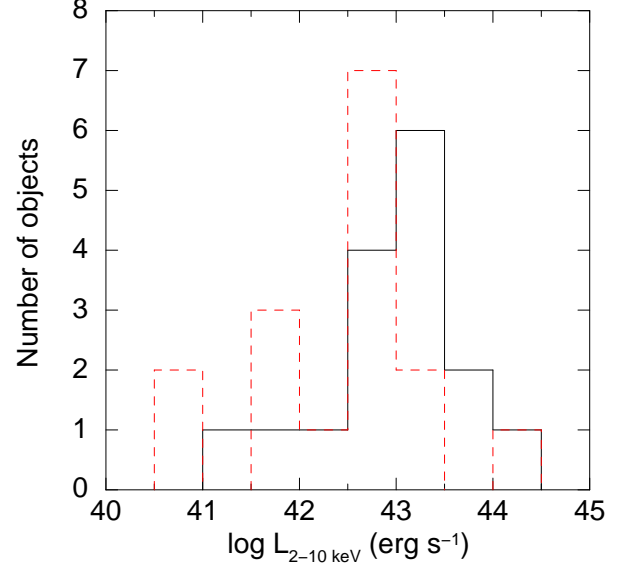


FIG. 6.— Distribution of the intrinsic luminosity in the 2–10 keV band for our sample (solid histogram) and the Seyfert 2 sample compiled by Bassani et al. (1999) with N_{H} in the range of $(0.6\text{--}20)\times 10^{23} \text{ cm}^{-2}$ (dashed histogram).

the range observed for starburst galaxies. This result indicates that thermal emission from a collisionally ionized plasma produced by starburst may contribute to the soft X-ray emission, and true values of scattering fraction for our sample would be smaller than the value calculated in this paper.

The distribution of $L_{\text{2-10}}^{\text{int}}/L_{[\text{O III}]}^{\text{int}}$ for our sample is shifted to higher values than that for other Seyfert 2s studied so far. $L_{[\text{O III}]}^{\text{int}}$ depends on the size of the NLR that is considered to be existed in the opening part of the torus. Thus, this result also indicates that the opening angle of the obscuring matter (or scattering optical depth) for our sample is smaller than those for other Seyfert 2, and there is a bias against such a type of AGN buried in a very geometrically thick torus in surveys that rely on optical emission.

We thank an anonymous referee for useful comments that improved the paper. This paper is based on observations obtained with *XMM-Newton*, an ESA science mission with instruments and contributions directly funded by ESA Member States and the USA (NASA). This research made use of the NASA/IPAC Extragalactic Database, which is operated by the Jet Propulsion Laboratory, California Institute of Technology, under contract with the National Aeronautics and Space Administration. This work is supported by Grants-in-Aid for Scientific Research 20740109 (Y.T.) and 21244017 (H.A.) from the Ministry of Education, Culture, Sports, Science, and Technology of Japan.

Facilities: *XMM-Newton*

REFERENCES

Anders, E., & Grevesse, N. 1989, *Geochim. Cosmochim. Acta*, 53, 197

Antonucci, R. 1993, *ARA&A*, 31, 473

Awaki, H., Koyama, K., Inoue, H., & Halpern, J. 1991, *PASJ*, 43, 195

Awaki, H., Murakami, H., Ogawa, Y., & Leighly, K. M. 2006, *ApJ*, 645, 928

Bassani, L., et al. 1999, *ApJS*, 121, 473

Bassani, L., et al. 2006, *ApJ*, 636, L65

Beckmann, V., Gehrels, N., Favre, P., Walter, R., Courvoisier, T. J.-L., Petrucci, P.-O., & Malzac, J. 2004, *ApJ*, 614, 641

Beckmann, V., Gehrels, N., Shrader, C. R., & Soldi, S. 2006, *ApJ*, 638, 64

Bianchi, S., & Guainazzi, M. 2007, in *AIP Conf. Ser.* 924, *The Multicolored Landscape of Compact Objects and Their Explosive Origins*, ed. T. di Salvo et al. (New York: AIP), 822

Bianchi, S., Guainazzi, M., & Chiaberge, M. 2006, *A&A*, 448, 499

Brandt, W. N., & Hasinger, G. 2005, *ARA&A*, 43, 827

Cappi, M., et al. 2006, *A&A*, 446, 459

Cash, W. 1979, *ApJ*, 228, 939

Comastri, A. 2004, in *Supermassive Black Holes in the Distant Universe*, ed. A. J. Barger (Dordrecht: Kluwer), 245

Comastri, A., Setti, G., Zamorani, G., & Hasinger, G. 1995, *A&A*, 296, 1

Costero, R., & Osterbrock, D. E. 1977, *ApJ*, 211, 675

David, L. P., Jones, C., & Forman, W. 1992, *ApJ*, 388, 82

De Rosa, A., Bassani, L., Ubertini, P., Panessa, F., Malizia, A., Dean, A. J., & Walter, R. 2008, *A&A*, 483, 749

Dong, X., Zhou, H., Wang, T., Wang, J., Li, C., & Zhou, Y. 2005, *ApJ*, 620, 629

Evans, D. A., Worrall, D. M., Hardcastle, M. J., Kraft, R. P., & Birkinshaw, M. 2006, *ApJ*, 642, 96

Fanaroff, B. L., & Riley, J. M. 1974, *MNRAS*, 167, 31

Foschini, L., et al. 2002, *A&A*, 392, 817

Gilli, R., Comastri, A., & Hasinger, G. 2007, *A&A*, 463, 79

Guainazzi, M., & Bianchi, S. 2007, *MNRAS*, 374, 1290

Guainazzi, M., Fabian, A. C., Iwasawa, K., Matt, G., & Fiore, F. 2005a, *MNRAS*, 356, 295

Guainazzi, M., Matt, G., & Perola, G. C. 2005b, *A&A*, 444, 119

Heckman, T. 1995, *ApJ*, 446, 101

Heckman, T. M., Ptak, A., Hornschemeier, A., & Kauffmann, G. 2005, *ApJ*, 634, 161

Helou, G., Soifer, B. T., & Rowan-Robinson, M. 1985, *ApJ*, 298, L7

Ho, L. C., Filippenko, A. V., & Sargent, W. L. W. 1997, *ApJS*, 112, 315

Isobe, N., Makishima, K., Tashiro, M., & Hong, S. 2005, *ApJ*, 632, 781

Kaastra, J. S. 1992, *An X-Ray Spectral Code for Optically Thin Plasmas* (Internal SRON-Leiden Report, updated version 2.0)

Kalberla, P. M. W., Burton, W. B., Hartmann, D., Arnal, E. M., Bajaja, E., Morras, R., & Pöppel, W. G. L. 2005, *A&A*, 440, 775

Kauffmann, G., et al. 2003, *MNRAS*, 346, 1055

Keel, W. C., de Grijp, M. H. K., Miley, G. K., & Zheng, W. 1994, *A&A*, 283, 791

King, A. 2005, *ApJ*, 635, 121

Kinkhabwala, A., et al. 2002, *ApJ*, 575, 732

Kiuchi, G., Ohta, K., Akiyama, M., Aoki, K., & Ueda, Y. 2006, *ApJ*, 647, 892

Kraft, R. P., Birkinshaw, M., Hardcastle, M. J., Evans, D. A., Croston, J. H., Worrall, D. M., & Murray, S. S. 2007, *ApJ*, 659, 1008

Landi, R., et al. 2007, *ApJ*, 669, 109

Liedahl, D. A., Osterheld, A. L., & Goldstein, W. H. 1995, *ApJ*, 438, L115

Magdziarz, P., & Zdziarski, A. A. 1995, *MNRAS*, 273, 837

Markwardt, C. B., Tueller, J., Skinner, G. K., Gehrels, N., Barthelmy, S. D., & Mushotzky, R. F. 2005, *ApJ*, 633, L77

Matt, G. 2002, *MNRAS*, 337, 147

Matt, G., Bianchi, S., D'Ammando, F., & Martocchia, A. 2004, *A&A*, 421, 473

Mewe, R., Gronenschild, E. H. B. M., & van den Oord, G. H. J. 1985, *A&AS*, 62, 197

Mulchaey, J. S., et al. 1994, *ApJ*, 436, 586

Netzer, H., Mainieri, V., Rosati, P., & Trakhtenbrot, B. 2006, *A&A*, 453, 525

Polletta, M., Bassani, L., Malaguti, G., Palumbo, G. G. C., & Caroli, E. 1996, *ApJS*, 106, 399

Ranalli, P., Comastri, A., & Setti, G. 2003, *A&A*, 399, 39

Sako, M., Kahn, S. M., Paerels, F., & Liedahl, D. A. 2000, *ApJ*, 543, 115

Sazonov, S., Revnivtsev, M., Krivonos, R., Churazov, E., & Sunyaev, R. 2007, *A&A*, 462, 57

Schurch, N. J., Roberts, T. P., & Warwick, R. S. 2002, *MNRAS*, 335, 241

Shinozaki, K., Miyaji, T., Ishisaki, Y., Ueda, Y., & Ogasaka, Y. 2006, *AJ*, 131, 2843

Shu, X. W., Wang, J. X., Jiang, P., Fan, L. L., & Wang, T. G. 2007, *ApJ*, 657, 167

Smith, D. A., & Done, C. 1996, *MNRAS*, 280, 355

Trinchieri, G., Rampazzo, R., Chiosi, C., Grutzaubach, R., Marino, A., & Tantalo, R. 2008, *A&A*, 489, 85

Trinchieri, G., Sulentic, J., Pietsch, W., & Breitschwerdt, D. 2005, *A&A*, 444, 697

Tueller, J., et al. 2008, *ApJ*, 681, 113

Turner, T. J., George, I. M., Nandra, K., & Mushotzky, R. F. 1997, *ApJS*, 113, 23

Ueda, Y., Akiyama, M., Ohta, K., & Miyaji, T. 2003, *ApJ*, 598, 886

Ueda, Y., et al. 2007, *ApJ*, 664, L79

Veron-Cetty, M. P., & Veron, P. 2006, *A&A*, 455, 773

Watson, M. G., et al. 2009, *A&A*, 493, 339

Winter, L. M., Mushotzky, R. F., Tueller, J., & Markwardt, C. 2008, *ApJ*, 674, 686

Worsley, M. A., et al. 2005, *MNRAS*, 357, 1281

Yee, H. K. C., & Oke, J. B. 1978, *ApJ*, 226, 753

Young, A. J., Wilson, A. S., & Shopbell, P. L. 2001, *ApJ*, 556, 6